Solar Physics (2024) 299:144
https://doi.org/10.1007/s11207-024-02386-9

RESEARCH

Impact of Magnetic and Flow Fields on Penumbrae and Light Bridges of Three Leading Sunspots in an Active Region

R. Kamlah[1,2] · M. Verma[1] · C. Denker[1] · N. Huang[3] · J. Lee[3] · H. Wang[3]

Received: 28 March 2024 / Accepted: 30 September 2024 / Published online: 15 October 2024

Abstract

This study investigates penumbrae and light bridges based on photospheric and chromospheric flow fields and photospheric magnetic fields in active region NOAA 13096. The improved High-resolution Fast Imager (HiFI+) and the GREGOR Infrared Spectrograph (GRIS) acquired high-resolution imaging and spectropolarimetric data at the 1.5-meter GREGOR solar telescope at the Observatorio del Teide, Izaña, Tenerife, Spain. Background-Subtracted Activity Maps (BaSAMs) have been used to locate areas of enhanced activity, Local Correlation Tracking (LCT) provides horizontal proper motions, and near-infrared full-Stokes polarimetry offers access to magnetic fields and line-of-sight velocities. The results show that the decaying active region is characterized by a triangular region between the three leading, positive-polarity sunspots with unfavorable conditions for penumbra formation. This region has a spongy appearance in narrow-band Hα images, shows signs of enhanced activity on small spatial scales, is free of divergence centers and exploding granules, lacks well-ordered horizontal flows, has low flow speeds, and is dominated by horizontal magnetic fields. Umbral cores are inactive, but the interface between pores and penumbral filaments often shows enhanced activity. Moat flows and superpenumbrae are almost always observed, when penumbral filaments are present, even in very small penumbral sectors. However, evidence of the moat flow can also be seen around pores, surviving longer than the decaying penumbral filaments. Light bridges have mainly umbral temperatures, reaching quiet-Sun temperatures in some places, show strong intensity variations, and exhibit weak photospheric horizontal flows, while narrow-band Hα flow maps show substantial inflows.

Keywords Photosphere · Chromosphere · Active regions · Sunspots · Image restoration · Instrumentation and data management

✉ R. Kamlah
rkamlah@aip.de

[1] Leibniz-Institut für Astrophysik Potsdam (AIP), An der Sternwarte 16, 14482 Potsdam, Germany

[2] Universität Potsdam, Institut für Physik und Astronomie, Karl-Liebknecht-Straße 24/25, 14476 Potsdam, Germany

[3] New Jersey Institute of Technology (NJIT), University Heights, 07102-1982 Newark, NJ, USA

1. Introduction

Solar active regions consist of a variety of features caused by rising magnetic flux with various field strengths, lifetimes, and spatial dimensions. Magnetic knots are granule-sized dark patches caused by relatively weak field strengths in the order of several 100 G and up to kilo-Gauss fields (Frazier and Stenflo 1978; Solanki 1993). Pores are larger in size with stronger fields in the range of 600 G – 1800 G (Sütterlin 1998; Verma and Denker 2014), which is approximately the observed field strength at the outer edge of the penumbra (Livingston 2002). The penumbra is the differentiating feature between pores and sunspots (Rucklidge, Schmidt, and Weiss 1995; Leka and Skumanich 1998). The field strength in the umbral cores of sunspots is in the range of 1800 G – 3700 G (Livingston 2002). Inflows can be observed at the borders of the pores, and the region connecting positive and negative-polarity typically contains large divergence centers caused by expanding granules. The transition from pore to sunspot is characterized by a variety of flows. For example, the moat flow (Vargas Domínguez et al. 2008), where the flow field is axially symmetric for sunspots with a fully developed penumbra (Löhner-Böttcher and Schlichenmaier 2013), exhibits a significant east–west asymmetry because of the sunspot's motion as a whole relative to the surroundings (Verma, Kummerow, and Denker 2018). This asymmetry can be modified by the tilt angle of the active region and the presence of plage in the surroundings. Even in light of these detailed descriptions of sunspot penumbrae, many questions remain open: How do penumbral filaments become a stable feature of sunspots? How are Evershed and moat flows connected to penumbral filaments and where do the flows terminate? Does the magnetic-field topology have an impact on penumbra formation and decay?

Light bridges appear as bright, long, and mostly narrow structures in the umbra. They are associated with the formation or decay of active regions, and recent simulations have shown that they form as a consequence of plasma intrusions at a certain depth, which are successively transported to the surface by upflows (Panja, Cameron, and Solanki 2021). According to Liu and Liu (2015), light bridges can be distinguished from the surrounding umbra by their weaker and more inclined fields. Therefore, it is necessary to consider the umbra and light bridges as two different systems. Jing et al. (2023) emphasized that the appearance and magnetic properties of light bridges depend on how much they are squeezed by the surrounding umbral magnetic field. The formation of light bridges has been linked to plasma ejections and chromospheric Hα surges (Roy 1973; Bharti, Joshi, and Jaaffrey 2007; Pietrow et al. 2022), adding them to the list of possible chromospheric heating mechanisms. After becoming visible at the surface, light bridges extend as a canopy structure into higher atmospheric layers. Several questions related to the relationship between sunspots and light bridges require further investigation: How do the appearance and evolution of light bridges affect the formation or decay of a penumbra? How do the physical properties of light bridges, such as temperature, change with the evolutionary stage of the sunspot?

This study investigates flows and magnetic fields in a complex active region with three leading sunspots containing light bridges, observed in several spectral regions covering the photosphere and chromosphere. Besides imaging data, spectropolarimetric data are analyzed. The observations and data processing are described in Section 2. The results of the data analysis are presented in Section 3, and their discussion follows in Section 4. Section 5 summarizes the findings of this study and emphasizes the need for further investigations of magnetic and flow fields in and around active regions.

2. Observations and Data Reduction

This section describes the recording, reduction, and analysis of high-resolution data from the 1.5-meter GREGOR solar telescope (Schmidt et al. 2012; Kleint et al. 2020) and synoptic data from the Solar Dynamics Observatory (SDO, Pesnell, Thompson, and Chamberlin 2012). In addition, it includes details on instruments, observing settings, and methods.

2.1. Observations

The high-resolution observations were carried out with the GREGOR telescope at Observatory del Teide, Izaña, Tenerife, Spain from 07:44 UT to 09:14 UT on 2022 September 9. The GREGOR Adaptive Optics System (GAOS, Berkefeld et al. 2012) provided real-time image correction of images and spectra. The updated "sTools" data processing pipeline (Kuckein et al. 2017) was used for image processing and image restoration. The observations focused on the leading part of the active region NOAA 13096. The region was classified by the *SolarMonitor* (Gallagher, Moon, and Wang 2002) web service[1] as a β-region according to the Mount Wilson classification (Hale et al. 1919). The GREGOR observations covered the three leading, positive-polarity sunspots with a partial penumbra, while the trailing negative-polarity sunspot with a complete penumbra was not included because of the limited field-of-view (FOV) of the GREGOR instruments and the required high cadence, which ruled out taking a mosaic of the active region. At the time of the observations, the active region was located at a heliocentric angle corresponding to $\mu = \cos\theta = 0.77$.

Synoptic data were provided by the Helioseismic and Magnetic Imager (HMI, Scherrer et al. 2012; Schou et al. 2012) onboard SDO. Standard data processing routines were used for the conversion of Level 1.0 to Level 1.5 data. Accordingly, the initial pixel scale of $0.5''$ pixel^{-1} of HMI data was adjusted to $0.6''$ pixel^{-1}. Further processing of HMI continuum images and magnetograms was carried out as described in Beauregard, Verma, and Denker (2012) and Verma (2018), which includes the correction for solar differential rotation. Figure 1 displays continuum images and magnetograms at the beginning and end of the high-resolution observations. The FOV is $120'' \times 120''$ or 200×200 pixels, and the heliocentric-Cartesian coordinates are given for the center of the FOV. The continuum and magnetograms were recorded at a cadence of 45 s. The magnetograms are displayed in the range of $\pm$ 1000 G. Geometrical foreshortening was not corrected, since the FOV is small. A four-day time-series of continuum images and magnetograms with a one-hour cadence is provided as online material using 08:00 UT on 2022 September 9 as the reference time.

2.1.1. Improved High-Resolution Fast Imager

The improved High-resolution Fast Imager (HiFI+, Denker et al. 2023a) has six imaging channels for high-resolution solar observations. The instrument successfully passed commissioning and science verification in early 2022 and has since then entered routine observations as one of GREGOR's facility instruments. This is one of the first case studies utilizing HiFI+ as a primary data source. The six channels feature various filters, which cover diagnostically important spectral regions, enabling synchronized high-cadence photospheric and chromospheric observations. Sets of 500 short-exposure images are acquired at frame rates of 49 Hz and 100 Hz depending on the camera model (Imager sCMOS and Imager M-lite 2M), but only the best 100 images are kept for image restoration. Details of the interference filters and of the detectors and their spectral coverage are listed in Table 1.

[1] www.solarmonitor.org.

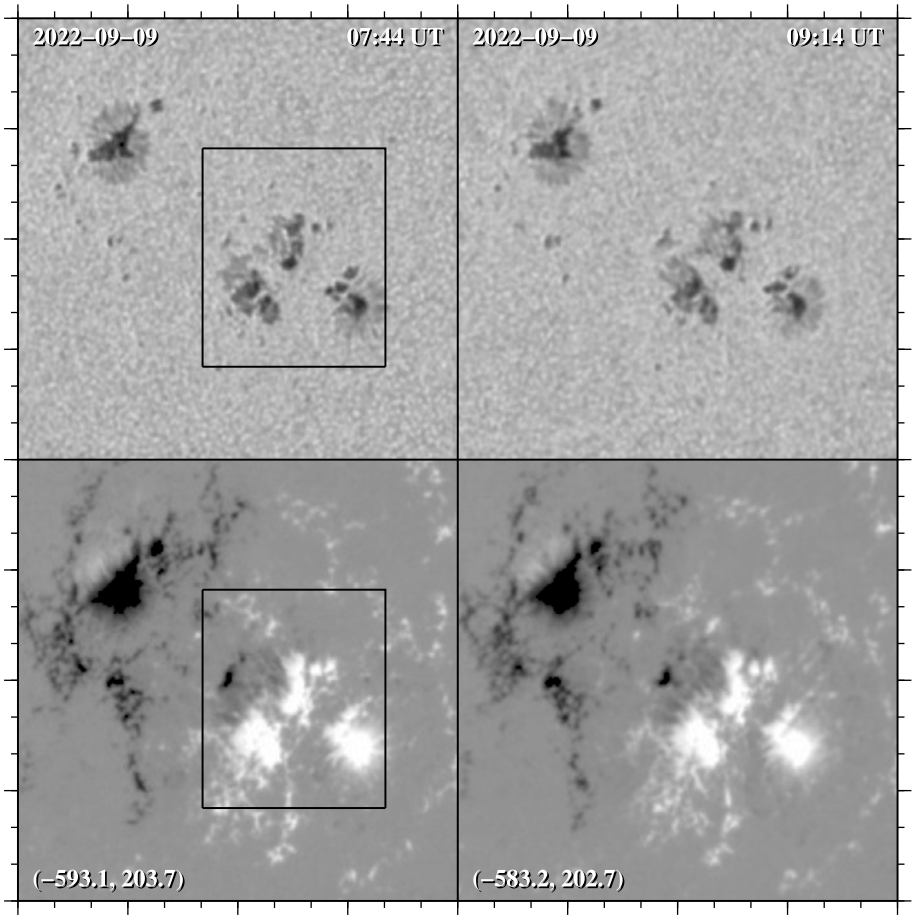

Figure 1 Synoptic HMI continuum images (top) and magnetograms (bottom) showing the evolution of active region NOAA 13096 from 07:44 UT (left) to 09:14 UT (right) on 2022 September 9. The FOV is $120'' \times 120''$ (major tick marks are separated by $30''$), and the heliocentric-Cartesian coordinates provided in the bottom-left corners of the magnetogram panels refer to the center of the FOV. The magnetograms are displayed in the range of ± 1000 G, where positive and negative polarities are shown in white and black, respectively. The black rectangles refer to the high-resolution observations with GREGOR (see Figure 2). A time-series of these data is provided as online material.

The two channels of the HiFI+ No. 1 Imager sCMOS camera system observe the photosphere in the Fraunhofer G-band (Sánchez Almeida et al. 2001) and in the blue continuum, which is strictly not pure continuum, but a spectral region where the line density is small (Denker et al. 2023a). The larger detector format and the camera interface result in an image acquisition rate of 49 Hz, and thus the cadence is 12 s for datasets used in image restoration. The four channels of the HiFI+ No. 2 and No. 3 Imager M-lite 2M camera systems observe chromospheric Ca II H images (Carlsson, De Pontieu, and Hansteen 2019), broad- and narrow-band chromospheric Hα images (Cauzzi et al. 2009; Leenaarts, Carlsson, and Rouppe van der Voort 2012; de la Cruz Rodríguez et al. 2019), and photospheric TiO images (Riethmüller et al. 2008). The image acquisition rate for these cameras is 100 Hz, and thus the cadence is 6 s for datasets used in image restoration. The Ca II H camera is located

Table 1 Characteristics of HiFI+ interference filters and cameras (see Tables 1 & 2 in Denker et al. 2023a).

	Ca II H	G-band	Blue continuum	Hα	TiO
Wavelength λ	396.8 nm	430.7 nm	450.6 nm	656.3 nm	705.8 nm
Passband $\Delta\lambda$	1.080 nm	1.120 nm	1.150 nm	0.750 nm	0.946 nm
Diffraction limit λ/D	0.057″	0.062″	0.065″	0.094″	0.101″
Max. transmission	63.8%	54.4%	64.5%	70.0%	68.8%
Plate scale	4.25″ mm^{-1}			8.50″ mm^{-1}	
Pixel scale	0.025″ pixel^{-1}	0.028″ pixel^{-1}		0.050″ pixel^{-1}	
FOV	48.2″ × 30.8″	70.7″ × 59.6″		76.5″ × 60.5″	
Number of pixels	1936 × 1216	2560 × 2160		1536 × 1216	
Frame rate	100 Hz	49 Hz		100 Hz	

in the blue arm of HiFI+ so that the full detector size can be used because of the smaller plate scale. In the red arm of HiFI+, a smaller part of the detector is used because the beam diameter is limited to 100″. A Halle Lyot filter with a bandpass of 60 pm is used to isolate the line core of the strong chromospheric Hα absorption line.

An overview of HiFI+ observations is presented in Figure 2 displaying Ca II H, G-band, blue continuum, broad- and narrow-band Hα, and TiO speckle-restored images. The data were recorded at about 08:35 UT under good seeing conditions. The common region-of-interest (ROI), which encompasses three small sunspots with rudimentary penumbrae surrounded by various pores, is used for further data analysis.

2.1.2. GREGOR Infrared Spectrograph

The spectropolarimetric data were taken with the GREGOR Infrared Spectrograph (GRIS, Collados et al. 2012), a slit-spectrograph capable for full Stokes vector polarimetry. GRIS was updated in 2022, when two spectral channels for multi-wavelength observations were introduced, facilitating spectropolarimetric observations in the 1.0 – 1.8 μm range and spectroscopic observations in the 2.0 – 2.3 μm range (Quintero Noda et al. 2022; Regalado Olivares et al. 2022). The spectropolarimetric observations on 2022 September 9 focused on the 1083 nm spectral range, which covers three magnetically sensitive spectral lines, that is, the photospheric Si I line at 1082.7 nm (Bard and Carlsson 2008), the deep photospheric Ca I line at 1083.9 nm, and the chromospheric He I triplet at 1083.0 nm (Avrett, Fontenla, and Loeser 1994). The observations were carried out using the long-slit mode. The number of spectral points was $n = 1010$, and the spectral sampling was 1.79 pm pixel^{-1}. Two scans were taken with 400 scan steps. The step size was about 0.13″. The pixel scale along the slit was about 0.13″ pixel^{-1}. This resulted in a FOV of about 52.0″ × 56.6″. The integration time used for each slit position was 100 ms with ten accumulations at each scan step. Each scan took approximately 40 min. The first and second scans began at 07:44 UT and 08:35 UT, respectively. However, only the second scan is discussed in the following because the AO lost lock during the scan, resulting in a displacement of the observed FOV.

2.2. Data Reduction

2.2.1. Improved High-Resolution Fast Imager

The HiFI+ data were split into two time-series covering the time periods from 07:44 UT to 08:24 UT and from 08:35 UT to 09:14 UT due to a gap in the observations. Each set of 100

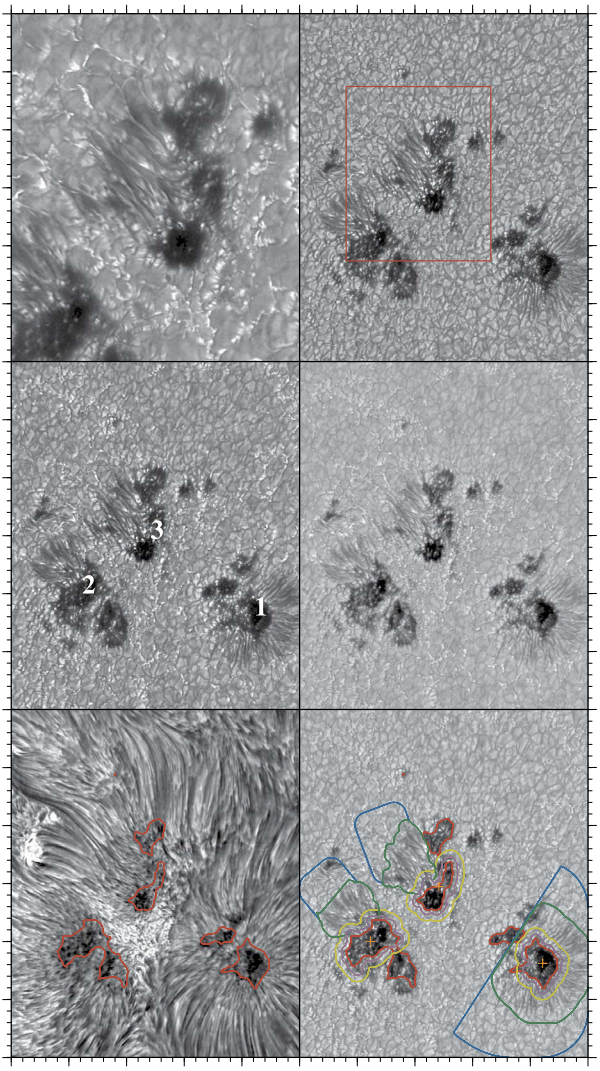

Figure 2 Speckle-restored images of three sunspots obtained by the six HiFI+ cameras at about 08:35 UT on 2022 September 9, that is, Ca II H (top-left), G-band (top-right), blue continuum (middle-left), broad-band Hα (middle-right), narrow-band Hα (bottom-left), and TiO (bottom-right) images. A common ROI of $50'' \times 60''$ (major tick marks are separated by $10''$) was extracted from the full FOV, except for the Ca II H image, where the ROI covers only $25'' \times 30''$. The red rectangle in the G-band image indicates the location of the Ca II H FOV. The red contours in the narrow-band Hα and TiO images outline the umbrae based on the TiO image, where an intensity threshold of $0.7\, I/I_0$ of the normalized quiet-Sun intensity was used. The contours in the bottom-right panel refer to umbra borders (purple), inflow regions at umbra borders (yellow), penumbrae (green), moat flow regions (blue), which were used to determine flow velocities. The orange crosses indicate the center of the umbrae. A time-series of these data is provided as online material.

short-exposure images was restored with the triple correlation or speckle masking technique (Lohmann, Weigelt, and Wirnitzer 1983; Weigelt and Wirnitzer 1983; de Boer 1993; von der Lühe 1993). The sTools data processing pipeline provides an interface to the Kiepenheuer Institute Speckle Interferometry Package (KISIP, Wöger and von der Lühe 2008; Wöger, von der Lühe, and Reardon 2008). The restored HiFI+ images were normalized such that the quiet-Sun intensity is unity. Rigid image motion was removed using the two-dimensional cross-correlation between the images and the average image of the time-series. Applying a Lee filter (Lee 1986) smoothes these images and removes the signature of the granulation so that only the position of the major sunspots enters in the cross-correlation. Differential image motion was removed with a destretching algorithm using a 128×128-pixel kernel in the first pass and a 64×64-pixel kernel in the second pass. A sliding average of nine images, centered on the image to be destretched, was used as a reference. Finally, a subsonic filter is applied

to the aligned and destretched image cube, taking into consideration the respective plate scales, cadences, and cut-off velocities. The cut-off velocities were chosen as 4 km s^{-1} for photospheric time-series and 15 km s^{-1} for chromospheric time-series. This step removes intensity variations caused by, for example, the five-minute oscillations.

The G-band time-series was used as a reference to align (translation and rotation) the blue continuum, broad-band Hα, and TiO time-series, since the information content of the mainly photospheric images is similar. Image restoration with Multi-Object Multi-Frame Blind Deconvolution (MOMFBD, Löfdahl 2002; van Noort, Rouppe van der Voort, and Löfdahl 2005) requires mechanical alignment of the broad- and narrow-band Hα channels with high accuracy. The technical details for the precise alignment of the cameras are described in Section 2.3 of Denker et al. (2023a). As a consequence, no additional alignment step is needed for the narrow-band Hα time-series. Finally, the smaller FOV of the Ca II H time-series made use of the locations of two sunspots and one pore within the reduced FOV. In addition, the AO lock point jumped 10 min before the end of the first time-series, introducing a shift of the FOV larger than the cumulative shifts due to random image motions throughout the time-series. All these factors limited the common FOV of the time-series to $55'' \times 65''$. However, for display purposes, this FOV was further cropped to $50'' \times 60''$ and $25'' \times 30''$ for Ca II H as shown in Figure 2.

The concept of Background-subtracted Solar Activity Maps (BaSAMs) was introduced by Denker and Verma (2019). These maps are computed to detect variations in and around sunspots and pores and to identify locations where significant intensity and magnetic field changes occur. This technique collapses an entire time-series into a two-dimensional map, subtracting an average map from individual maps before averaging the resulting maps. Two-dimensional BaSAMs are an effective quantitative tool for visualizing and identifying locations where significant changes occur, as demonstrated by Verma et al. (2012) and Verma et al. (2020), where BaSAMs were applied to HMI LOS magnetograms and ultraviolet images acquired with the Atmospheric Imaging Assembly (AIA, Lemen et al. 2012) on board SDO. Recently, Kamlah et al. (2023) showed the first application of BaSAMs to high-resolution data of three pores and a light bridge, and Denker et al. (2023b) extended the BaSAM concept to imaging spectroscopic data.

Horizontal proper motions are measured using Local Correlation Tracking (LCT, November and Simon 1988), which is applied to the high-resolution data as described in Verma and Denker (2011). The horizontal velocities for each pixel in the FOV are computed over image tiles with a size of $2.2'' \times 2.2''$, corresponding to about 1600 km $\times$ 1600 km on the solar surface. A Gaussian kernel with full-width-at-half-maximum (FWHM) of 1200 km is applied to the image tiles to track granule-sized structures. The size of the sampling window and the width of the Gaussian kernel were kept the same in this study, regardless of the observed solar features and the chosen wavelength channel. Images, separated in time by $\Delta t = 6 \times 6$ s $= 36$ s (Ca II H, broad- and narrow-band Hα, TiO) and $\Delta t = 3 \times 12$ s $= 36$ s (blue continuum and G-band), are used for the LCT computation. The computed flow vectors are averaged over the duration of each time-series, that is, $\Delta T = 40$ min, which minimizes contributions by granules, revealing persistent flow patterns.

2.2.2. GREGOR Infrared Spectrograph

The initial GRIS data reduction takes place on-site using Version 8 of the GRIS data pipeline (Manuel Collados, private communication). This process includes several steps, such as dark-frame subtraction, flat-field correction, crosstalk removal, and calibration of the polarization modulator (Collados 1999). Subsequent data reduction steps, such as wavelength

calibration and correction for the spectrograph profile, among others, follow the descriptions provided in Verma et al. (2016, 2018). The "Stokes Inversion based on Response functions" (SIR, Ruiz Cobo and del Toro Iniesta 1992) code was employed to invert spectra of the second scan. The data analysis focuses on the photospheric Si I line at 1082.7 nm ($g_{\rm eff} = 1.5$). The initial model for the Si I line encompasses the optical depth range of $+1.0 \leq \log \tau \leq -5.4$. A limb-darkening factor was incorporated in line with Equation 10 in Pierce, Slaughter, and Weinberger (1977). A constant macroturbulence value of 1 km s^{-1} was assumed. In addition, a fixed stray light contribution of one percent was applied, with this choice acting as a lower limit (Balthasar et al. 2016). The inversions yielded the temperature stratification using three nodes $T(\tau)$, while the total magnetic flux density $B_{\rm tot}$, the magnetic-field inclination γ and azimuth ϕ, and the Doppler velocity $v_{\rm LOS}$ remained constant with height, that is, each of these physical parameters has only one node. Pixels with a circular and linear degree of polarization below 0.2% were excluded from any subsequent magnetic-field analysis. The magnetic azimuth ambiguity was solved by using the best matching Spaceweather HMI Active Region Patch (SHARP, Bobra et al. 2014) as initial estimate and then smoothing the azimuth map with iteratively larger windows from a size of 3×3 pixels up to a size of 23×23 pixels. Azimuth angles were flipped by 180°, if in 70% of the cases the scalar product between the azimuth angle and all other azimuth angles in the window was larger than 180°.

In addition to the SIR results, the LOS velocities and line-core intensities of the Si I, Ca I, and He I lines were derived using the Fourier phase method (Schmidt, Stix, and Wöhl 1999). For the He I triplet, only the red component was fitted. The average velocity of dark umbral cores served as the reference for the zero point of the LOS velocities. Figure 3 compiles a sample of slit-reconstructed GRIS maps, depicting the mean continuum intensity, the Si I line-core intensity, the Si I LOS velocity, and the He I line-core intensity for the second GRIS scan starting at 08:35 UT. All three sunspots of leading polarity are contained in the GRIS FOV.

3. Results

In this section, the morphology and temporal evolution of the active region are studied using time-series of synoptic and high-resolution data. The magnetic connectivity of the active region is investigated, and horizontal proper motions and LOS velocities are combined to study the three-dimensional flow field in and around the sunspots.

3.1. Morphology

The combination of spectral bands observed with HiFI+ allows us to analyze the solar atmosphere at different heights, ranging from the photosphere to the chromosphere. The inclusion of SDO HMI continuum images and magnetograms further extends the analysis. Doppler velocities can be studied by using spectropolarimetric GRIS data covering the deep photosphere, the photosphere, and the chromosphere.

On 2022 September 6, active region NOAA 13096 was close to the eastern limb and was identified as an α-region according to the Hale classification (Hale et al. 1919) and as an Hsx-region according to the McIntosh classification (McIntosh 1990). The leading positive-polarity sunspot was almost completely encircled by a penumbra and was followed by two small pores of positive polarity. By the next day, the active region had grown in size, with the trailing negative-polarity sunspot forming a penumbra and new pores appearing in the

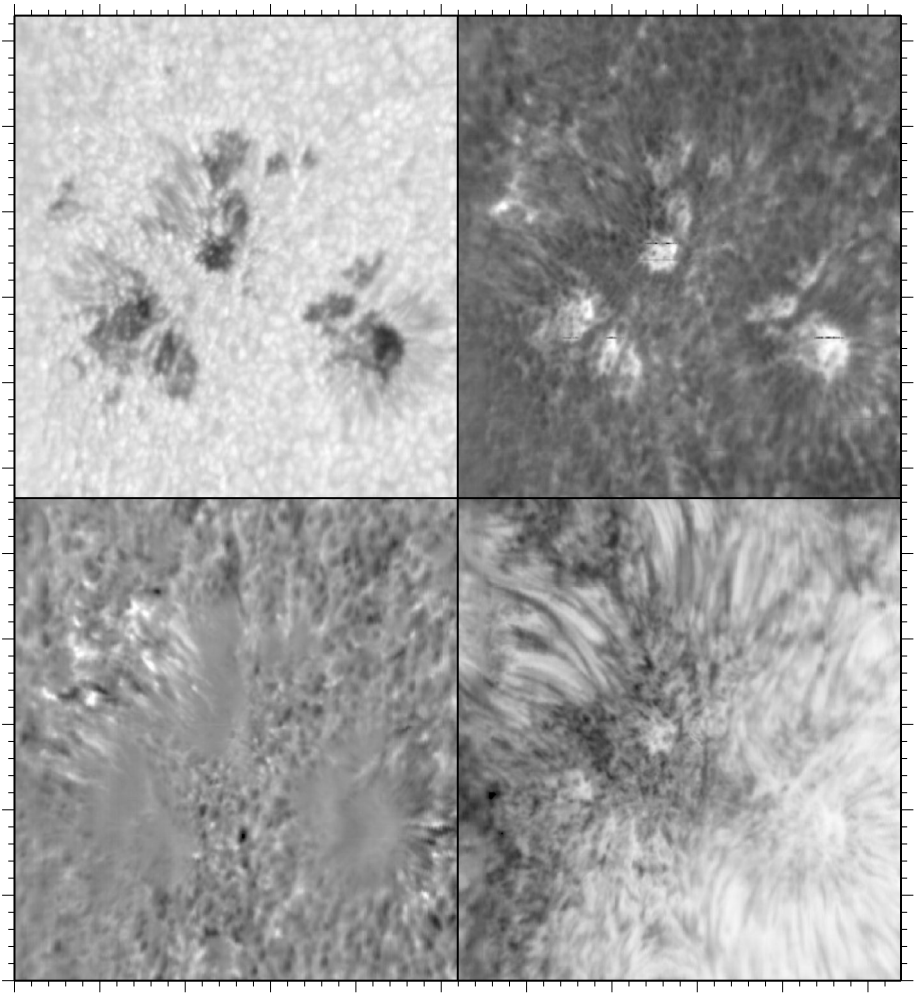

Figure 3 Slit-reconstructed GRIS maps at 08:35 UT of the mean continuum intensity (top-left), the Si I line-core intensity (top-right), the Si I LOS velocity (bottom-left), and the He I line-core intensity (bottom-right). The physical parameters are scaled as follows: continuum intensity $I/I_0 \in [0.5,\ 1.1]$, Si I line-core intensity $I/I_0 \in [0.3,\ 0.6]$, Si I LOS velocity ± 2 km s^{-1}, and He I line-core intensity $I/I_0 \in [0.5,\ 1.0]$. The FOV is $52.0'' \times 56.6''$, and major tick marks are separated by $10''$.

leading part. The typical separation of opposite polarities, as seen in regions with new flux emergence, was present, with a clockwise rotation of the trailing sunspot.

On September 8, the continuous flux emergence between the two polarities of the active region led to its classification as a β- and Dso-region. Visual inspection of HMI and HiFI+ time series (see animations of Figures 1 and 2) already revealed that the leading positive-polarity sunspot was surrounded by the moat flow (Vargas Domínguez et al. 2008), which became more pronounced once the sunspot moved into the center of a supergranule at about 10:00 UT. The two smaller sunspots of leading polarity showed signs of the moat flow only where the rudimentary penumbra had formed. The trailing sunspot also appeared to be located in the center of a supergranule a day later, which was accompanied by an increase in

moat flow. A C-class flare occurring in an adjacent active region at 17:00 – 18:00 UT coincided with a simplification of the magnetic configuration, that is, mixed polarities separated and a negative-polarity patch to the east of the leading sunspots started to decay.

By September 9, active region NOAA 13096 reached its maximum size, with 130 millionths of a solar hemisphere. The leading polarity had gained two more sunspots with rudimentary penumbra at about 02:00 UT. Throughout its entire evolution, from its appearance on the limb until the beginning of the high-resolution observations, no penumbra formed in the region between the leading sunspots of the same polarity facing each other (see Künzel 1969). The two polarities of the region continued to separate, leading to the formation of more pores of negative polarity. High-resolution GREGOR observations on September 9 followed the evolution of the region. By September 10, the region was classified as a Dai-region. On the following day, the leading-polarity sunspots had disappeared, leaving only a trailing sunspot with a partial penumbra. Pores in the trailing region persisted until September 12. By September 16, just before the region rotated off the disk, only patches of opposite polarity were still visible in magnetograms, with no evidence of dark features or pores in the continuum.

3.1.1. Photospheric Evolution

For a more structured discussion of the leading part of active region NOAA 13096, the high-resolution GREGOR observations on September 9 are divided into three smaller regions-of-interest (ROIs), highlighted in the middle-left panel of Figure 2. The overall appearance of the high-resolution photospheric observations (that is, G-band, blue continuum, Hα broad-band, and TiO images) is quite similar. All dark umbrae show umbral dots, and the FOV is covered by small-scale bright points, as seen in all photospheric channels except the blue continuum channel. The umbral dots and bright points are more pronounced in TiO images, where bright points are seen extending from sunspot No. 3 towards the trailing negative polarity region, which is not covered by the FOV. In addition, the dynamics and variability in the FOV are also well captured by the Hα broad-band channel, despite the lower contrast compared to the other photospheric channels.

The leading sunspot No. 1 is surrounded by a penumbra, except for the inner part facing sunspots No. 2 and 3. In the region between the three sunspots, none of them formed a penumbra at any time. In addition, two pores are located in the vicinity of sunspot No. 1, one in the north at coordinates (40″, 24″) and the other at (38″, 20″), separated from the sunspot by a light bridge. During the GREGOR observations, the penumbra remained stable and no major changes were observed.

Sunspot No. 2 at coordinates (12″, 20″) has a rudimentary penumbra, which formed along the eastern edge of the sunspot, limited to a segment of about 4″. The sunspot is separated from its neighboring pore at coordinates (14″, 17″) by a light bridge and has two dark knots below at coordinates (10″, 11″) and (6″, 14″), which remained stable during the GREGOR observations.

Sunspot No. 3 also developed only a rudimentary penumbra at the eastern edge of the sunspot. The sunspot umbra split up at 8:13 UT and formed a light bridge at coordinates (24″, 36″). Besides the formation of a light bridge, this ROI appears in a stable configuration and small features remain visible during GREGOR observations, that is, two tiny pores at coordinates (30″, 38″) and (34″, 38″).

3.1.2. Chromospheric Evolution

In the chromospheric broad-band Ca II H images, the typical photospheric granulation pattern is still visible. The FOV includes sunspot No. 3 and partially sunspot No. 2. The in-

tergranular lanes appear mostly bright in regions directly associated with flux emergence (bottom-left quadrant of the FOV) or in the regions between the two sunspots (bottom-right quadrant of the FOV). The overall size and shape of the observed features in the lower chromosphere are consistent with the photospheric morphology, including a light bridge that is clearly visible in the umbra of sunspot No. 3. During the observations, the penumbral filaments of sunspot No. 3 became longer. The dark lane in the light bridge of sunspot No. 2, which is partially obscured, is also visible.

In narrow-band Hα observations (see the bottom-left panel of Figure 2), the scene appears drastically different compared to the lower atmospheric layers. The sunspot umbrae, indicated by red contour lines, are barely visible. An intensity threshold of $0.7\,I_0$ for the TiO intensity was chosen for the umbral contours. The FOV is dominated by filamentary structures. Most prominent is the bright triangular central region between the three positive-polarity sunspots, that is, the spongy region between sunspots No. 1, 2, and 3 and a small bright region at coordinates (4″, 36″). The leading sunspot No. 1 is almost completely surrounded by radial superpenumbral filaments, which are not fully formed around the sunspots No. 2 and 3. In addition, a dark persistent filament is present in the region between sunspot No. 2 and 3, extending to the trailing negative-polarity sunspot. This dark filament constantly interacts with the small bright region mentioned above. To the south and west, where a more finely structured pattern was observed, elongated filaments are present, which are absent in the southeast. Similar to sunspots No. 1 and 2, the sunspot No. 3 never developed a filamentary structure towards the central region between the three sunspots. Chromospheric filaments extend to the east and north of the sunspot No. 3 at the location of the rudimentary penumbra. However, the filaments in this direction are cut off by the small bright region mentioned above. Despite the highly dynamic fine structure within the FOV, the overall position and shape of the dark cores, filamentary structure, and bright regions remain the same during the chromospheric high-resolution observations.

3.2. Background-Subtracted Activity Maps

The BaSAM results for the HiFI+ data $\langle |I - \langle I \rangle| \rangle$ are shown in Figure 4, using the same layout as in Figure 2. The angle brackets $\langle \ldots \rangle$ indicate a time-series average, and I refers to the intensity. The color scale from red to blue highlights regions of large and small variations, respectively. The individual maps show the combined results of the first and second time-series in a single map covering an ROI of $50'' \times 60''$, except for the top-left panel, where the Ca II H BaSAM is shown with an ROI of $25'' \times 30''$. Larger BaSAM values shown in red indicate stronger variations at that locations, while blue colors point to quieter regions.

3.2.1. Photosphere

The overall appearance of the photospheric BaSAMs is similar in all four photospheric channels: blue continuum, G-band, broad-band Hα, and TiO (Figure 4). The quietest regions are the umbral cores of the three sunspots as well as their neighboring pores, except for the broad-band Hα BaSAM. The granulation pattern is visible in all four photospheric channels and shows low to medium BaSAM values, with the strongest variations occurring at the umbral borders. While the umbral regions in the TiO and broad-band Hα BaSAMs are still the locations of the lowest values detected within the FOV, their patchy red and blue patterns make them appear more dynamic compared to the remaining photospheric observations.

The low signal within the penumbra on the western side of sunspot No. 1 indicates only small variations and therefore a stable configuration of the penumbra. The umbra of sunspot

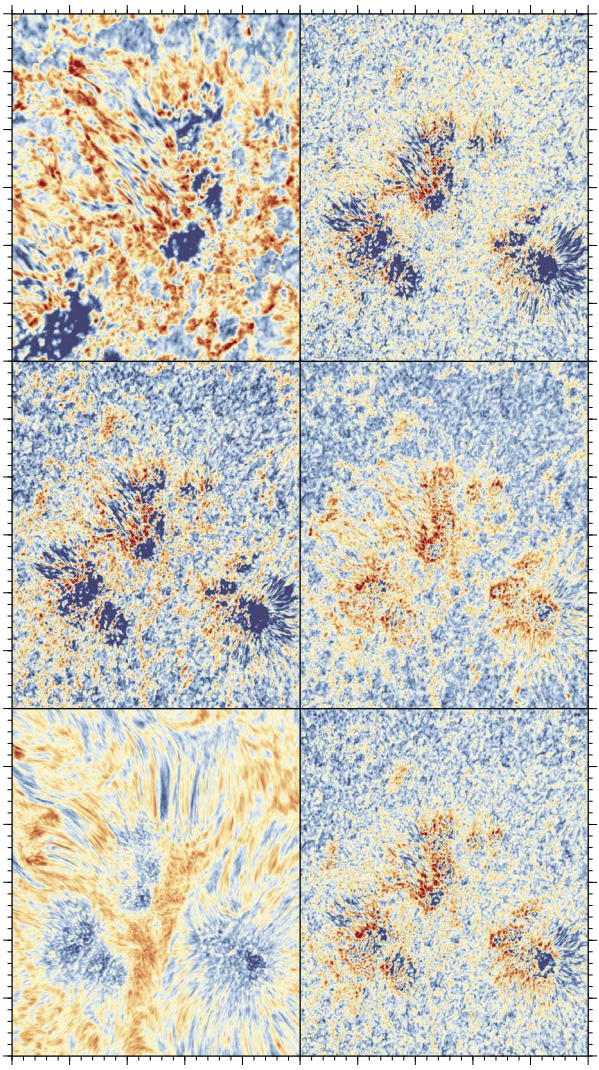

Figure 4 Combined BaSAMs based on the first and second time-series (07:44 – 08:24 UT and 08:35 – 09:14 UT) of speckle-restored HiFI+ images: Ca II H (top-left), G-band (top-right), blue continuum (middle-left), broad-band Hα (middle-right), narrow-band Hα (bottom-left), and TiO (bottom-right). A common ROI of $50'' \times 60''$ (major tick marks are separated by $10''$) was extracted from the full FOV, except for the Ca II H image, where the ROI covers only $25'' \times 30''$.

No. 1 does not contain many umbral dots or other features that could cause a signal in the photospheric BaSAMs. Only at the southern border of the sunspot No. 1, does the penumbra show a mixed pattern of high and low signals. In addition, large variations are associated with the neighboring pore at coordinates ($35''$, $20''$), the light bridge separating the sunspot from the pore, and the small pore in the north at coordinates ($40''$, $24''$).

The umbral borders of sunspot No. 2 and its neighboring pores are also locations of strong signals, while the rudimentary penumbra shows a mixed pattern of high and low signals. With increasing distance from the penumbra–umbra interface, parts of the rudimentary penumbra exhibit some of the lowest BaSAM values in the entire FOV. This is particularly evident in the G-band and blue continuum BaSAMs, where parts of the rudimentary penumbra are prominently displayed in dark blue color, while small patches associated with variations within the umbra are much more abundant and prominent in the broad-band Hα

and TiO BaSAMs. Strong variations were also detected at the location of the light bridge, especially near two small pores where the chevron-like light bridge begins on the eastern side of the sunspot.

The BaSAMs show that sunspot No. 3 contains the strongest variations in the FOV. In particular, the umbra-penumbra interface and parts of the penumbra are highlighted in dark red. However, the rudimentary penumbra also contains quieter areas in the middle of the penumbral filaments, which are highlighted in blue. In addition, the northern part of the umbra shows a very strong signal, indicating a highly dynamic interface with the penumbra at this location.

3.2.2. Chromosphere

The chromospheric Ca II H BaSAMs are very similar to the photospheric BaSAMs, with stronger signals mainly due to the higher contrasts of the small-scale brightenings, which are in most cases co-spatial in chromospheric and photospheric images (see Figure 2). The umbrae of sunspots No. 2 and 3 are clearly visible due to the very small variations. However, the umbral borders are characterized by strong BaSAM signals, indicating a very dynamic interface with the rudimentary penumbrae. In addition, the entire FOV of the zoomed-in Ca II H observations shows a mixed pattern of low, medium, and high signals, with strong variations appearing as filamentary extensions of the penumbral filaments. Alternating patterns of strong and weak signals characterize the rudimentary penumbrae of sunspots No. 2 and 3, especially at the penumbra–granulation interface.

Due to the drastic morphological differences observed in narrow-band Hα observations, the corresponding BaSAMs give a very different picture of the chromospheric activity. The FOV is dominated by elongated filamentary structures with strong variations. The umbrae are clearly visible in all three ROIs due to very low BaSAM values. In addition, the broad and elongated filament at coordinates (26″, 46″) is a persistent feature during the GREGOR observations. A second low-signal filamentary structure extends from sunspot No. 3 towards the trailing negative-polarity region. The southeast corner of the FOV contains a highly dynamic, fine-grained region, where elongated filaments are absent. The central region in between the three sunspots is characterized by a very strong signal and variations on small spatial scales. However, the regions with the strongest signals are located at coordinates (4″, 36″) and (1″, 53″) at the periphery of the FOV near the footpoints of the filaments. The superpenumbra associated with the rudimentary penumbrae of sunspots No. 2 and 3 causes a mixed pattern of high and low BaSAM signals. In contrast, the extended superpenumbra of sunspot No. 1 is characterized by lower BaSAM signals, indicating a more stable configuration.

3.3. Local Correlation Tracking

Horizontal proper motions were determined using LCT (November and Simon 1988; Verma and Denker 2011) for time-series of TiO, Ca II H, and narrow-band Hα images. Local cross-correlations were computed for images separated in time by 36 s. Only persistent flows were measured by averaging the individual flow maps over the duration of the time-series of approximately 40 min. Color-coded flow vectors are superimposed on the averaged image to indicate flow speed and direction. Since cross-correlations track contrast features in the sampling window, equating horizontal proper motions with plasma velocities has to be interpreted with caution. In the following, three flow maps are shown side by side for the first and second time-series, tracing the flow fields from the photosphere to the chromosphere.

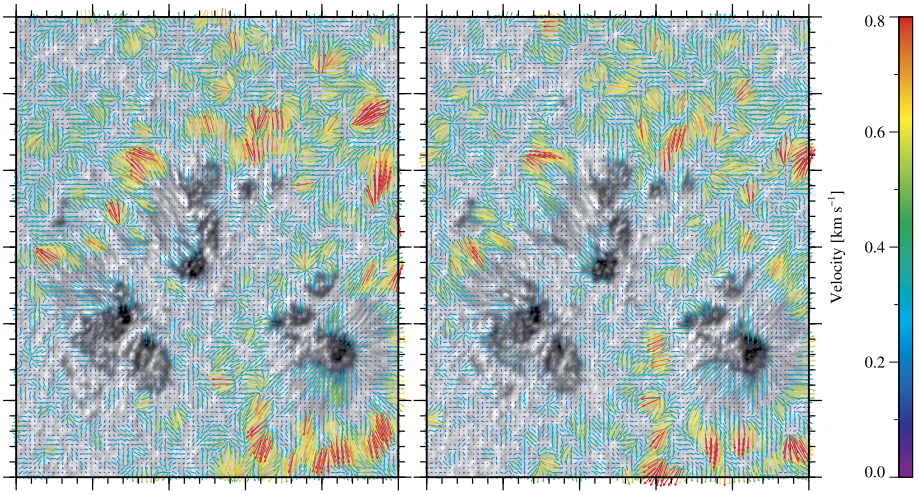

Figure 5 Two-dimensional flow maps based on TiO first (left) and second (right) time-series. The ROI covers $50'' \times 60''$, and major tick marks are separated by $10''$. Flow speeds are displayed in the range $0.0-0.8$ km s^{-1}.

3.3.1. Photosphere

The LCT results based on photospheric observations are very similar. Therefore, only the TiO LCT maps are shown in Figure 5. The FOV covers $50'' \times 60''$ with average flow speeds displayed in the range of $0.0-0.8$ km s^{-1}. The flow vectors are superimposed on the averaged TiO images for the corresponding time-series. In general, the horizontal proper motions detected in the first time-series are also recovered in the second time-series. However, the flow pattern appears more fragmented at lower flow speeds. The moat flow is present at every location with a (rudimentary) penumbra. Even some locations without penumbra show signs of moat flow, for example, the two small pores in the west of sunspot No. 3 or the region on the eastern side of sunspot No. 1. Divergence centers caused by granulation are present around the sunspots. However, strong divergence centers, which are typical of exploding/expanding granules in opposite-polarity regions (Bonet et al. 2005), are absent. Patternless divergence centers with increased flow speeds are present in the northwest corner of the FOV. In contrast, the divergence centers in the southeast corner of the FOV are inconspicuous and have much lower flow speeds. The central region between the three sunspots is devoid of any well-ordered motions or divergence centers, and only low flow speeds are detected. The animated version of Figure 2 can be used to visualize the persistent flows captured in the LCT maps of Figure 5.

More quantitative results of the flow speeds are summarized in Table 2 for the umbra, the border of the umbra, the penumbra, and the moat flow regions. The regions for which the flow speeds are computed are outlined in the bottom-right panel of Figure 2. In addition to the total flow field, the radial flows were computed, with respect to the center of the umbral cores. The mean values of the flow speed are given with the standard deviation, which reflects the variation of the flow speeds in the selected regions and should not be taken as a formal error estimate.

The most prominent flow is the moat flow around sunspot No. 1, which just starts outside the penumbra. The averaged velocity maps show a radial outflow with velocities of

Table 2 Averaged horizontal proper motions of the umbra, umbral border, penumbra, and moat region for the three ROIs. Mean and standard deviation of the LCT results are based on the combined TiO observations of the first and second time-series. Details on the LCT setup are given at the end of Section 2.2.1.

	No.	Total flow field	Radial flows
Umbra	1	(0.18 ± 0.10) km s^{-1}	(0.16 ± 0.10) km s^{-1}
	2	(0.14 ± 0.06) km s^{-1}	(0.10 ± 0.07) km s^{-1}
	3	(0.14 ± 0.09) km s^{-1}	(0.09 ± 0.08) km s^{-1}
Umbral border	1	(0.19 ± 0.11) km s^{-1}	(0.17 ± 0.12) km s^{-1}
	2	(0.14 ± 0.08) km s^{-1}	(0.08 ± 0.10) km s^{-1}
	3	(0.17 ± 0.10) km s^{-1}	(0.06 ± 0.11) km s^{-1}
Penumbra	1	(0.23 ± 0.15) km s^{-1}	(-0.06 ± 0.25) km s^{-1}
	2	(0.20 ± 0.15) km s^{-1}	(-0.06 ± 0.22) km s^{-1}
	3	(0.16 ± 0.13) km s^{-1}	(-0.03 ± 0.19) km s^{-1}
Moat	1	(0.43 ± 0.23) km s^{-1}	(-0.36 ± 0.27) km s^{-1}
	2	(0.32 ± 0.20) km s^{-1}	(-0.22 ± 0.26) km s^{-1}
	3	(0.38 ± 0.22) km s^{-1}	(-0.27 ± 0.26) km s^{-1}

(-0.36 ± 0.27) km s^{-1}. The moat flow is absent in the central region between the three sunspots. The Evershed flow in the penumbra of sunspot No. 1 has an average outflow speed of (-0.06 ± 0.25) km s^{-1}. Low inflow speeds of (0.17 ± 0.12) km s^{-1} are measured at the umbra–penumbra interface, which continue into the umbra with speeds (0.16 ± 0.10) km s^{-1}. The light bridge is devoid of strong horizontal motions and no signs of convective upwelling were found in its center. The location, where the light bridge connects to the plasma surrounding the sunspot, shows small inward motions that are not detected in the second time-series. Both pores near sunspot No. 1 are characterized by inflows at the umbra–granulation interface.

Strong horizontal proper motions are detected only in the moat region of sunspot No. 2, which are restricted to a narrow region at coordinates (5″, 28″), where the average outflow speed is (-0.22 ± 0.26) km s^{-1}. Otherwise, only small outflows of (-0.06 ± 0.22) km s^{-1} are measured in the penumbra, while inflows of (0.08 ± 0.10) km s^{-1} and (0.10 ± 0.07) km s^{-1} are determined at the border of the umbra and inside the umbra, respectively. The light bridge shows no signs of directed plasma motions, which excludes convective upwelling in the center of the light bridge. The small pore above the rudimentary penumbra of sunspot No. 2 at coordinates (6″, 34″) shows moderate inflows that become stronger during the second time-series.

Average outflows of (-0.27 ± 0.26) km s^{-1} and (-0.03 ± 0.19) km s^{-1} were measured for the moat flow and Evershed flow of sunspot No. 3, respectively. Average inflows of (0.06 ± 0.11) km s^{-1} and (0.09 ± 0.08) km s^{-1} were determined at the border of the umbra and within the umbra, respectively. The large horizontal proper motions north of the umbra of sunspot No. 1 and the neighboring two pores decreased during the second time-series.

3.3.2. Chromosphere

The results of applying LCT to the chromospheric Ca II H observations are shown in Figure 6. In general, the Ca II H flow maps are similar to the photospheric flow maps, with divergence centers caused by granulation and significant inflows and outflows associated with sunspots. In contrast to the generally decreasing photospheric flow speeds during the second time-series, the chromospheric Ca II H flow maps give the impression of increased flows.

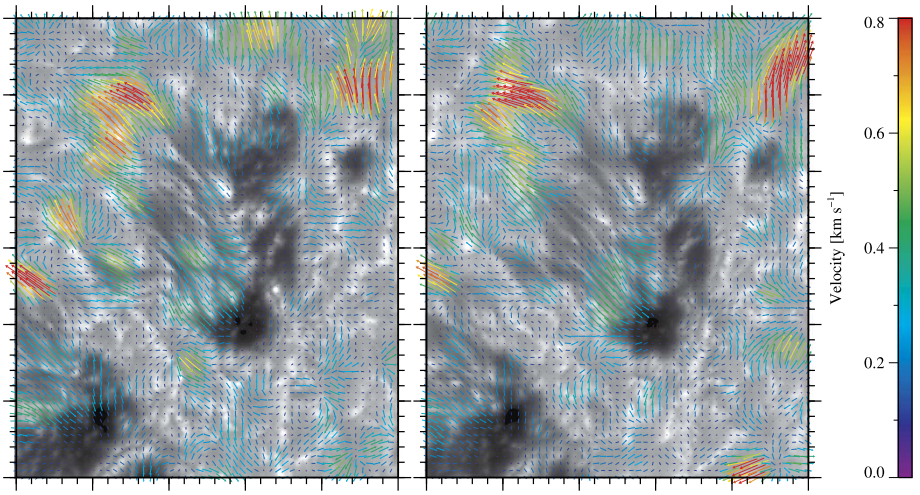

Figure 6 Two-dimensional flow maps based on the first (left) and second (right) Ca II H time-series. The ROI covers $25'' \times 30''$, and major tick marks are separated by $5''$. Flow speeds are displayed in the range $0.0-0.8\ \mathrm{km\,s^{-1}}$.

Due to the limited FOV of the Ca II H observations, only the flows at the northern and western border of the sunspot No. 2 can be studied. The light bridge is devoid of strong horizontal proper motions and outflows along the light bridge are missing. In agreement with photospheric flow maps, the strongest motions of sunspot No. 2 are located at the outer ends of the filaments in the rudimentary penumbra at coordinates ($4''$, $25''$). The average flow speed decreases at this location in the second time-series. The flow speeds are moderate in the region between the sunspots No. 2 and 3 and decrease significantly during the second time-series.

The inflows at the border of the umbra of sunspot No. 3 are enhanced at the location where the rudimentary penumbra has formed and appear slightly increased in the second time-series. The moat flow begins at the periphery of the rudimentary penumbra, and even single, isolated penumbral filaments show evidence of moat flow at their tips. In particular, strong outflows in excess of $0.5\ \mathrm{km\,s^{-1}}$ are associated with the small pore at coordinates ($23''$, $21''$), which intensify and become more confined in the second time-series.

The appearance of the chromospheric narrow-band Hα flow maps in Figure 7 differs significantly from the photospheric flow maps. Strong flows enter the FOV at coordinates ($43''$, $60''$), where they meet oppositely directed flows with moderate flow speeds at coordinates ($37''$, $54''$). Inflows surround the sunspot No. 1. The bright filament above the sunspot No. 3 at coordinates ($24''$, $47''$) shows strong and confined inflows that become even more confined in the second time-series. A strong eastward motion coincides with the bright patch at coordinates ($4''$, $36''$) and the associated dark filament at coordinates ($5''$, $44''$), where the flows increase significantly in the second time-series, especially along the dark filament. The bright central region between the three sunspots at coordinates ($22''$, $22''$) is characterized by low to moderate flow speeds, forming a front with flow vectors directed towards the sunspot No. 1.

The superpenumbra that partially surrounds the sunspot No. 1 shows an inward motion, which is characteristic of the inverse Evershed flow (Moore and Rabin 1985). These flows are significantly larger in a small region at coordinates ($44''$, $10''$). In general, the flows associated with the superpenumbra of this sunspot are the same in both time-series. The

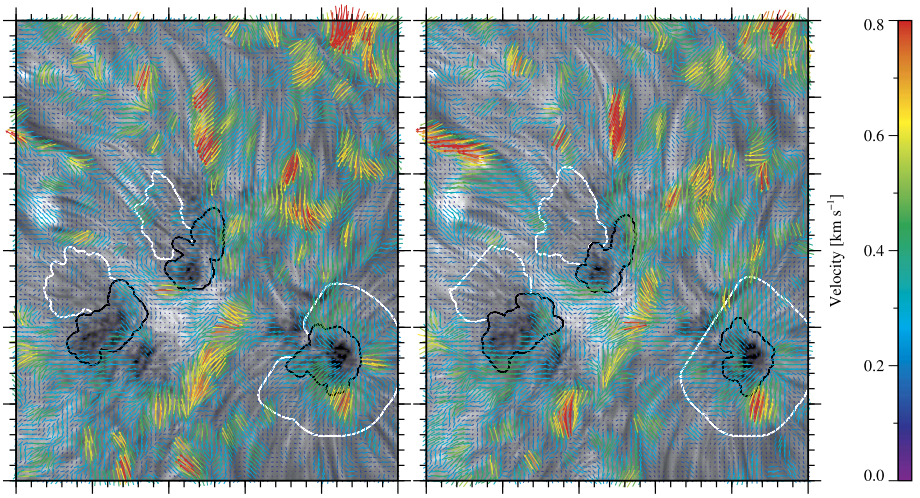

Figure 7 Two-dimensional flow maps based on the first (left) and second (right) narrow-band Hα time-series. The ROI covers $50'' \times 60''$, and major tick marks are separated by $10''$. Flow speeds are displayed in the range $0.0-0.8$ km s^{-1}. The black contours that outline the umbrae are based on the TiO image, where an intensity threshold of $0.7\,I/I_0$ of the normalized quiet-Sun intensity was used, and the white contours outline the penumbrae.

Table 3 Averaged horizontal proper motions of the umbra, umbral border, penumbra, and moat region for the three ROIs. Mean and standard deviation of the LCT results are based on the combined narrow-band Hα observations of the first and second time-series. Details on the LCT setup are given at the end of Section 2.2.1.

	No.	Total flow field	Radial flows
Umbra	1	(0.26 ± 0.11) km s^{-1}	(0.20 ± 0.13) km s^{-1}
	2	(0.20 ± 0.10) km s^{-1}	(0.03 ± 0.12) km s^{-1}
	3	(0.23 ± 0.10) km s^{-1}	(0.07 ± 0.14) km s^{-1}
Umbra border	1	(0.33 ± 0.15) km s^{-1}	(0.30 ± 0.14) km s^{-1}
	2	(0.20 ± 0.11) km s^{-1}	(0.03 ± 0.12) km s^{-1}
	3	(0.27 ± 0.14) km s^{-1}	(0.10 ± 0.16) km s^{-1}
Penumbra	1	(0.28 ± 0.13) km s^{-1}	(0.23 ± 0.14) km s^{-1}
	2	(0.11 ± 0.06) km s^{-1}	(-0.02 ± 0.08) km s^{-1}
	3	(0.16 ± 0.09) km s^{-1}	(-0.02 ± 0.08) km s^{-1}
Moat	1	(0.18 ± 0.11) km s^{-1}	(-0.03 ± 0.11) km s^{-1}
	2	(0.18 ± 0.10) km s^{-1}	(0.07 ± 0.15) km s^{-1}
	3	(0.21 ± 0.09) km s^{-1}	(-0.11 ± 0.15) km s^{-1}

rudimentary penumbra of the sunspot No. 2 shows no signs of the inverse Evershed flow. Overall, the horizontal proper motions within this ROI are small, with stronger inflows at the location of the light bridge and the umbral core at coordinates ($16''$, $16''$), with inflows becoming stronger in the second time-series. The flow pattern associated with the sunspot No. 3 shows much variation between the two time-series. The inverse Evershed flow is observed only in the northern part of the sunspot, mainly at locations with filamentary structure. In the southern part of the sunspot, the velocity vectors form streamlines around the umbra.

The chromospheric flow velocities corresponding to the photospheric ROIs outlined in the bottom-right panel of Figure 2 are summarized in Table 3. The velocities determined in the chromosphere are generally of lower magnitude than their photospheric counterparts. In particular, the radial flows in the direction of the center of the sunspots, indicated by the orange crosses in Figure 2, differ significantly in the moat flow region, with photospheric velocities exceeding those of the chromosphere. In contrast to the photospheric flows, the penumbral region of sunspot No. 1 and the moat region of sunspot No. 2 show an outward motion at chromospheric height with very low velocities.

3.4. Magnetic Fields

Magnetic fields and the sensitivity of certain spectral lines to them provide access to different atmospheric and magnetic-field parameters using inversion codes. In the following, the GRIS observations are studied with an emphasis on plasma temperatures and the orientation and strength of the photospheric magnetic field using the SIR inversion code.

The SIR code was used to derive the six physical parameters in Figure 8 for the Si I line. The slit-reconstructed continuum intensity image is very similar to the TiO observations discussed in Section 3.1.1, but the contrasts of the umbral dots and of the light bridges are reduced, giving the visual impression that the umbral cores are more densely filled by these features. The light bridges have predominantly umbral temperatures, with the exception of sunspot No. 1, where the temperatures of the light bridges are higher and reach quiet-Sun temperatures. The highest temperatures are found in the rudimentary penumbrae of sunspots No. 2 and 3, which even show small kernels of localized heating. The three sunspots are clearly separated in the map of the vertical component of the magnetic field strength B_z. An almost field-free region divides sunspots No. 2 and 3 from sunspot No. 1. This separation of the flux systems is repeated successively on the hierarchical level of the umbral cores, where light bridges serve as separators.

A patch of negative polarity region is present on the left side of sunspots No. 2 and 3, as also seen in the SDO magnetograms. Small-scale positive and negative polarity features are scattered around sunspot No. 1, which are the typical type II and III moving magnetic features (MMF, Harvey and Harvey 1973; Hagenaar and Shine 2005), respectively. The strongest horizontal component of the magnetic field strength $B_{\rm hor}$ is found around sunspots No. 2 and 3 in the region associated with the rudimentary penumbral filaments. In the region between sunspots No. 1, 2, and 3 $B_{\rm hor}$ is much stronger than B_z. The field inclination is mostly vertical in the sunspots with a gradual decrease when going from the dark umbral core to the penumbra-granulation border. The negative polarity region shows the presence of inclined field lines. The orientation of the field lines can be followed in the azimuth map. However, only for sunspot No. 1 do the field lines follow the full compass rose.

4. Discussion

This case study addresses the dynamic interplay of magnetic fields and plasma flows associated with three positive-polarity sunspots with rudimentary penumbrae and light bridges in active region NOAA 13096. The high-resolution observations are interpreted in the context of active-region decay in the following days. The decay process was atypical, since the observed leading polarity was less compact and fragmented earlier than the single sunspot in the trailing part of the active region.

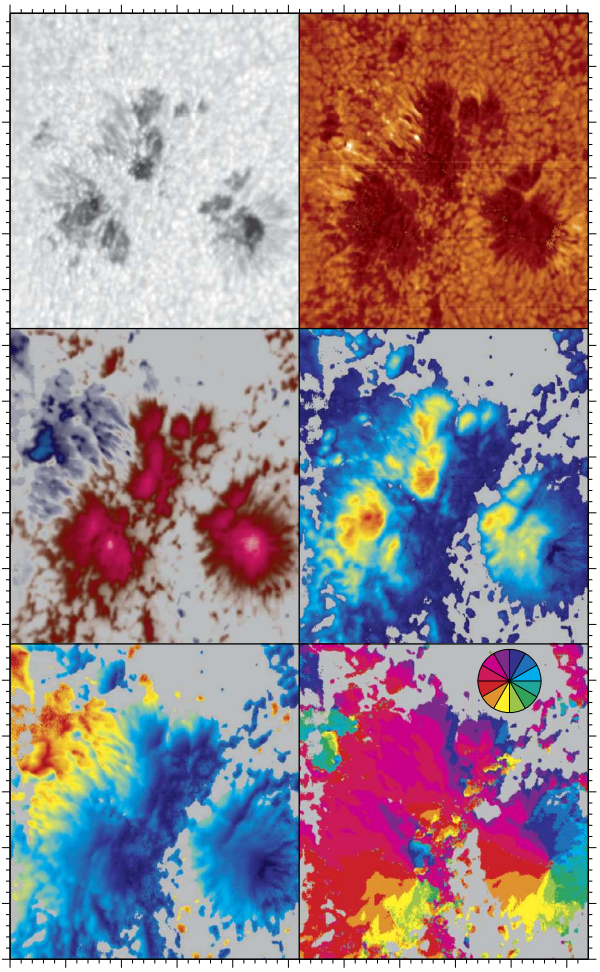

Figure 8 Maps of six physical parameters derived for the Si I line (from top-left to bottom right): continuum intensity in the range of (0.5 – 1.1) I_0, temperature in the range of 5500 K – 6000 K, vertical magnetic field strength B_z in the range of $\pm$ 2000 G (blue/red corresponds to negative/positive magnetic fields), horizontal magnetic field strength $B_{\rm hor}$ in the range of 0 G – 1800 G (rainbow color table), inclination in the range of 0° – 180° (rainbow color table), and azimuth in the range of 0° – 360° (color wheel in the upper-right corner indicates the direction of the magnetic fields). Regions with a degree of polarization below 0.2% are displayed in gray. The FOV is $52.0'' \times 56.6''$, and major tick marks are separated by $10''$.

The penumbra formation begins in the leading part, followed by the trailing sunspot. The three positive-polarity sunspots show no signs of rotation, while the trailing negative-polarity sunspot rotated clockwise (Howard 1990; D'Silva and Howard 1994; Kutsenko, Abramenko, and Litvishko 2023) until a southward drift began. A magnetic flux concentration in a small, unnumbered active region to the south of the observed active region produced a C-class flare on 2022 September 8, which coincided with a simplification of the magnetic configuration of active region NOAA 13096. However, the system remained globally stable, but with many small-scale changes. The region between the leading and trailing sunspots was devoid of exploding or expanding granules, as often found in bipolar regions with flux emergence (Bonet et al. 2005; Kamlah et al. 2023).

Penumbra formation is still an elusive topic and depends strongly on the topology of the active region and the structure of the local plasma flows. At the beginning of the GREGOR observations, only one of the three leading sunspots had a penumbra while the other two had rudimentary penumbrae (Watanabe, Kitai, and Otsuji 2014). However, a penumbra never formed in the central region, where sunspots of the same polarity face each other (Künzel 1969; Murabito et al. 2021). Several studies (Shimizu, Ichimoto, and Suematsu 2012; Ro-

mano et al. 2013, 2014; Murabito et al. 2016; Romano et al. 2020) have emphasized that inclined photospheric magnetic field lines can be formed by shifting chromospheric field lines with typical tilts of 40° – 80° down to the photosphere. However, this penumbra formation scenario requires a canopy to confine the chromospheric field lines. The mostly vertical fields in the central region between the three sunspots prevent such a canopy and consequently preclude penumbra formation in this region (Murabito et al. 2021; Lindner et al. 2023). Furthermore, the latter authors showed that the analysis of the magnetic topology in the deep photospheric layers alone is not a reliable indicator for the presence of a penumbra, which is consistent with the missing horizontal magnetic-field component of sunspot No. 1 (see the middle-right panel of Figure 8).

If the photospheric Evershed effect is driven by a siphon flow, magnetoconvection, or a mixture of both is still an ongoing debate, although recent observations favor magnetoconvection (Murabito et al. 2016). The three-dimensional topography of sunspots supports the theory of mass motion and wave propagation from the photosphere to the corona along field lines (Staude 1999; Solanki 2003; Khomenko and Collados 2015). The dominant drivers of mass motion are typically the Evershed and inverse Evershed flows in the photosphere and chromosphere, respectively, with the latter starting at a height of about 500 km (Boerner and Kneer 1992). The penumbrae of the three leading sunspots show the Evershed effect (Evershed 1909), which transports material from the umbra along penumbral filaments into the surroundings. The average LCT velocities determined are close to zero and thus significantly lower than the penumbral velocities determined in other studies (i.e., greater than 1.5 $\mathrm{km\,s^{-1}}$, Molowny-Horas 1994; Verma et al. 2018; Wang et al. 2018; Márquez, Sánchez Almeida, and Bonet 2006) or found in simulations (i.e., 3 – 4 $\mathrm{km\,s^{-1}}$, Rempel 2015). The low penumbral flow speeds are interpreted as the imminent decay of the penumbrae. The variability detected in BaSAMs emphasizes the changes associated with inflows at the umbral borders. However, the penumbra of sunspot No. 1 and the rudimentary penumbrae of sunspots No. 2 and 3 show some of the strongest BaSAM signals during the observations, which becomes much weaker at the periphery of the rudimentary penumbrae. These patches of low flow speeds are located at the interface between the penumbra and the moat flow, which causes the signal to increase with distance. The chromospheric Ca II H observations show inflows at the border of the pore, which are comparable to photospheric flows, and a divergence region in the middle of the rudimentary penumbra with inflows in the inner penumbra and outflows in the outer parts (Deng et al. 2007; Verma and Denker 2011).

In magnetograms, the moat regions appear to be enhanced after the umbrae have moved to the center of the supergranules. The present flow maps show that the moat flow is closely associated with rudimentary and regular penumbrae. Several studies have determined horizontal velocities of the moat flow in the range of 0.5 $\mathrm{km\,s^{-1}}$ – 1.0 $\mathrm{km\,s^{-1}}$ (Muller and Mena 1987; Shine et al. 1996; Bonet et al. 2005; Sobotka and Roudier 2007), which is consistent with the present measurements in the range of 0.2 $\mathrm{km\,s^{-1}}$ – 1.0 $\mathrm{km\,s^{-1}}$. Moving magnetic features, transporting magnetic flux from the umbra to the supergranular cell boundaries, reach velocities up to 2 $\mathrm{km\,s^{-1}}$ – 3 $\mathrm{km\,s^{-1}}$ (Shine et al. 1996; Hagenaar and Shine 2005). These velocities are typically measured by applying feature tracking methods to small-scale magnetic features. In contrast, LCT follows contrast variations within a sampling window, which contains contributions from various features. These contrast changes are not always related to plasma motions, and even if a close relationship to plasma motions exists, LCT methodd can significantly underestimate plasma velocities (Verma, Steffen, and Denker 2013). Thus, the present results do not argue against higher flow speeds observed for moving magnetic features. Due to the late evolutionary stage of the sunspots, the flow speed within the moat significantly exceeds the outflows in the penumbra. The moat flow is visible in

the flow maps up to about 4 Mm beyond the periphery of the penumbra, which is a much smaller value than previously reported (i.e., 10 Mm – 20 Mm, Sheeley 1972; Brickhouse and Labonte 1988) and contradicts the tendency of more mature sunspots to have more extended moat regions (Sobotka and Roudier 2007). However, Löhner-Böttcher and Schlichenmaier (2013) concluded that moat radii are independent of sunspot radii, which was further supported by Verma, Kummerow, and Denker (2018). The present study supports the finding that moat and Evershed flows are firmly linked to the presence of a penumbra. Even the smallest patches of penumbra are accompanied by these outflows. In summary, the moat flow dissolves and disappears after the decay of the penumbra. However, spectropolarimetric observations with higher cadence are needed to study the cessation of the moat flow as a function of time, which is an interesting science case for high-resolution telescopes equipped with imaging spectropolarimeters.

All observed umbrae contain umbral dots, which are however less prominent in BaSAMs due to their shorter lifetimes of 15 min – 60 min and dimensions of 80 km – 400 km (Beckers and Schröter 1968; Koutchmy and Adjabshirzadeh 1981; Lites et al. 1991; Sobotka, Brandt, and Simon 1997; Denker 1998). Moreover, they are stable features, at least in the central part of the umbrae. The chromospheric Ca II H BaSAMs and LCT maps closely resemble those of the blue continuum observations. Strong variations within the umbrae are not detected, although some intrusions of bright points from the periphery, which only give weak signals. However, bright intergranular lanes in between the positive-polarity sunspots and extending out to the trailing part of NOAA 13096 are very prominent in the BaSAMs.

In the chromospheric narrow-band Hα BaSAMs, the umbrae are clearly visible as regions with only small variations. However, the central T-shaped part in between the positive-polarity sunspots on the other hand stands out for its bright and spongy appearance, causing a strong signal in the BaSAMs and highlighting the strong variability on small spatial scales. This phenomenon is called "moss" in EUV images (Berger et al. 1999) and is caused by thermal conduction from coronal loops with temperatures of $(3-5) \times 10^6$ K situated above a plage. In fact, this location is associated with the footpoint region of a coronal loop. Berger et al. (1999) emphasized that the spongy appearance is caused by chromospheric jets (Wang et al. 1998; Mulay et al. 2016; Iijima and Yokoyama 2017) and spicules (Moore et al. 1977; Tsiropoula et al. 2012) interspersed with EUV emission. The misalignment with the underlying magnetic elements can be confirmed in the present study. Despite the apparent increase in activity, the superpenumbral flows in this region are low, if present at all.

While the leading sunspot No. 1 is almost completely surrounded by superpenumbra, the other two leading sunspots developed only rudimentary superpenumbral structures at the locations where also rudimentary penumbra had formed in the photosphere. The BaSAMs indicate a rather stable configuration of the superpenumbra around sunspot No. 1 by its alternating red and blue filamentary structure. In addition, LCT flow maps show an inward motion for sunspot No. 1, which is not aligned with the superpenumbral filaments. The dark filaments, seen as elongated dark blue structures in BaSAMs, extending from sunspot No. 3 to the trailing negative-polarity sunspot, appear in a stable configuration, while inhibiting major horizontal proper motion.

5. Conclusions

The combination of ground-based high-resolution observations of different spectral regions and thus different atmospheric heights with synoptic SDO full-disk data made a comprehensive analysis of the active region NOAA 13096 possible, scrutinizing the photospheric Evershed flow and the chromospheric inverse Evershed flow. The fragmentation of the leading

sunspots before the trailing sunspot is a rather atypical behavior for active region evolution. The decay process was studied in terms of plasma flows and connectivity to the surroundings using LCT and BaSAMs.

The imminent decay of the active region is characterized by the relatively low Evershed flows. Only one of the leading positive-polarity sunspots has a superpenumbra, while rudimentary superpenumbrae formed only at the locations where photospheric rudimentary penumbrae already existed, which were facing the trailing negative-polarity sunspot. Exploding or expanding granules, which are typically present in the center of bipolar regions, are not observed. Light bridges, present in all three leading sunspots, do not cause a temperature increase. However, they appear as field-free regions in horizontal and vertical magnetic field maps. In addition, no convective outflows were found along the light bridges. In chromospheric narrow-band Hα observations, features associated with EUV moss were found in the form of a bright spongy region. This region was slightly displaced with respect to magnetic features in lower atmospheric layers, in agreement with previous descriptions of this phenomenon.

Further analysis of emerging and decaying active regions is needed to better understand the difference between regions with and without field-aligned flows. In particular, the transition from emergence to decay needs to be studied in more detail to clarify the role of light bridges in the decay process. How does the magnetic field weaken in these regions, which eventually become field-free? In addition, the influence of the low-lying magnetic canopy over light bridges and its relation to the umbral magnetic field and the plasma flows requires closer scrutiny. To get a coherent picture of the interplay between features caused by strong magnetic fields (i.e., sunspots and pores) and features related to them (i.e., light bridges and umbral dots), more case studies are required, combining different spatial and temporal scales and covering different atmospheric heights in multi-wavelength observations. As more and more high-resolution imaging and spectropolarimetric data become publicly accessible in archives of for example, the GREGOR solar telescope, Daniel K. Inouye Solar Telescope (DKIST), and the Swedish Solar Telescope (SST), targeted searches to answer some of the open questions on active-region evolution become possible.

Acknowledgments SDO HMI data are provided by the Joint Science Operations Center – Science Data Processing. This research has made use of NASA's Astrophysics Data System (ADS). DeepL Write was used in copy editing (spelling, grammar, and readability) of the manuscript.

Author contributions The individual contributions by the authors are listed according to the Contributor Roles Taxonomy (credit.niso.org). Robert Kamlah: conceptualization, formal analysis, investigation, software, validation, visualization, and writing – original draft; Meetu Verma: conceptualization, formal analysis, funding acquisition, investigation, methodology, project administration, software, supervision, validation, visualization, and writing – review & editing; Carsten Denker: data curation, formal analysis, funding acquisition, investigation, methodology, project administration, software, supervision, validation, visualization, and writing – review & editing; Nengyi Huang: investigation, and writing – review & editing; Jeongwoo Lee: investigation, funding acquisition, project administration, supervision, and writing – review & editing; Haimin Wang: investigation, funding acquisition, project administration, supervision, and writing – review & editing.

Funding This study was supported by grants DE 787/5-1 and VE 1112/1-1 of the Deutsche Forschungsgemeinschaft (DFG). In addition, the support by the European Commission's Horizon 2020 Program under grant agreements 824064 (ESCAPE – European Science Cluster of Astronomy & Particle physics ESFRI research infrastructures) and 824135 (SOLARNET – Integrating High Resolution Solar Physics) is highly appreciated. This study was supported by NASA grants 80NSSC20K0182, 80NSSC20K1282, and AGS-2114201.

Data Availability No datasets were generated or analysed during the current study.

Declarations

Competing interests The authors declare no competing interests.

References

Avrett, E.H., Fontenla, J.M., Loeser, R.: 1994, Formation of the solar 10830 Å line. In: Rabin, D.M., Jefferies, J.T., Lindsey, C. (eds.) *Infrared Solar Physics*, *IAU Symp.* **154**, 35. DOI.

Balthasar, H., Gömöry, P., González Manrique, S.J., Kuckein, C., Kavka, J., Kucera, A., Schwartz, P., Vaskova, R., Berkefeld, T., Collados, M., Denker, C., Feller, A., Hofmann, A., Lagg, A., Nicklas, H., Schlichenmaier, R., Schmidt, D., Schmidt, W., Sigwarth, M., Sobotka, M., Solanki, S.K., Soltau, D., Staude, J., Strassmeier, K.G., Volkmer, R., von der Lühe, O., Waldmann, T.: 2016, Spectropolarimetric observations of an arch filament system with the GREGOR solar telescope. *Astron. Nachr.* **337**, 1050. DOI.

Bard, S., Carlsson, M.: 2008, Constructing computationally tractable models of Si I for the 1082.7 nm transition. *Astrophys. J.* **682**, 1376. DOI.

Beauregard, L., Verma, M., Denker, C.: 2012, Horizontal flows concurrent with an X2.2 flare in active region NOAA 11158. *Astron. Nachr.* **333**, 125. DOI.

Beckers, J.M., Schröter, E.H.: 1968, The intensity, velocity and magnetic structure of a sunspot region. I: observational technique; properties of magnetic knots. *Solar Phys.* **4**, 142.

Berger, T.E., De Pontieu, B., Fletcher, L., Schrijver, C.J., Tarbell, T.D., Title, A.M.: 1999, What is moss? *Solar Phys.* **190**, 409. DOI.

Berkefeld, T., Schmidt, D., Soltau, D., von der Lühe, O., Heidecke, F.: 2012, The GREGOR adaptive optics system. *Astron. Nachr.* **333**, 863. DOI.

Bharti, L., Joshi, C., Jaaffrey, S.N.A.: 2007, Observations of dark lanes in umbral fine structure from the Hinode solar optical telescope: evidence for magnetoconvection. *Astrophys. J. Lett.* **669**, L57.

Bobra, M.G., Sun, X., Hoeksema, J.T., Turmon, M., Liu, Y., Hayashi, K., Barnes, G., Leka, K.D.: 2014, The Helioseismic and Magnetic Imager (HMI) vector magnetic field pipeline: SHARPs – space-weather HMI active region patches. *Solar Phys.* **289**, 3549. DOI.

Boerner, P., Kneer, F.: 1992, High resolution observations of the evershed flow. *Astron. Astrophys.* **259**, 307.

Bonet, J.A., Márquez, I., Muller, R., Sobotka, M., Roudier, T.: 2005, Phase diversity restoration of sunspot images. II. Dynamics around a decaying sunspot. *Astron. Astrophys.* **430**, 1089. DOI.

Brickhouse, N.S., Labonte, B.J.: 1988, Mass and energy flow near sunspots. I. Observations of moat properties. *Solar Phys.* **115**, 43.

Carlsson, M., De Pontieu, B., Hansteen, V.H.: 2019, New view of the solar chromosphere. *Annu. Rev. Astron. Astrophys.* **57**, 189. DOI.

Cauzzi, G., Reardon, K., Rutten, R.J., Tritschler, A., Uitenbroek, H.: 2009, The solar chromosphere at high resolution with IBIS. IV. Dual-line evidence of heating in chromospheric network. *Astron. Astrophys.* **503**, 577. DOI.

Collados, M.: 1999, High resolution spectropolarimetry and magnetography. In: Schmieder, B., Hofmann, A., Staude, J. (eds.) *Third Advances in Solar Physics Euroconference: Magnetic Fields and Oscillations*, *ASP Conf. Ser.* **184**, 3.

Collados, M., López, R., Páez, E., Hernández, E., Reyes, M., Calcines, A., Ballesteros, E., Díaz, J.J., Denker, C., Lagg, A., Schlichenmaier, R., Schmidt, W., Solanki, S.K., Strassmeier, K.G., von der Lühe, O., Volkmer, R.: 2012, GRIS: the GREGOR infrared spectrograph. *Astron. Nachr.* **333**, 872. DOI.

de Boer, C.R.: 1993, Speckle-Interferometrie und ihre Anwendungen auf die Sonnenbeobachtung. PhD thesis, Georg-August Universität Göttingen.

de la Cruz Rodríguez, J., Leenaarts, J., Danilovic, S., Uitenbroek, H.: 2019, STiC: a multiatom non-LTE PRD inversion code for full-Stokes solar observations. *Astron. Astrophys.* **623**, A74. DOI.

Deng, N., Choudhary, D.P., Tritschler, A., Denker, C., Liu, C., Wang, H.: 2007, Flow field evolution of a decaying sunspot. *Astrophys. J.* **671**, 1013.

Denker, C.: 1998, Speckle masking imaging of sunspots and pores. *Solar Phys.* **180**, 81.

Denker, C., Verma, M.: 2019, Background-subtracted Solar Activity Maps. *Solar Phys.* **294**, 71. DOI.

Denker, C., Verma, M., Pietrow, A.G.M., Kontogiannis, I., Kamlah, R.: 2023b, Spectral Background-subtracted Activity Maps. *Res. Notes Am. Astron. Soc.* **7**, 224. DOI.

Denker, C., Verma, M., Wiśniewska, A., Kamlah, R., Kontogiannis, I., Dineva, E., Rendtel, J., Bauer, S., Dionies, M., Önel, H., Woche, M., Kuckein, C., Seelemann, T., Pal, P.S.: 2023a, Improved high-resolution fast imager. *J. Astron. Telesc. Instrum. Syst.* **9**, 015001. DOI.

D'Silva, S., Howard, R.F.: 1994, Sunspot rotation and the field strengths of subsurface flux tubes. *Solar Phys.* **151**, 213. DOI.

Evershed, J.: 1909, Radial movement in sunspots. *Mon. Not. Roy. Astron. Soc.* **69**, 454.

Frazier, E.N., Stenflo, J.O.: 1978, Magnetic, velocity and brightness structure of solar faculae. *Astron. Astrophys.* **70**, 789.

Gallagher, P.T., Moon, Y.-J., Wang, H.: 2002, Active-region monitoring and flare forecasting I. Data processing and first results. *Solar Phys.* **209**, 171. DOI.

Hagenaar, H.J., Shine, R.A.: 2005, Moving magnetic features around sunspots. *Astrophys. J.* **635**, 659.

Hale, G.E., Ellerman, F., Nicholson, S.B., Joy, A.H.: 1919, The magnetic polarity of sun-spots. *Astrophys. J.* **49**, 153. DOI.

Harvey, K., Harvey, J.: 1973, Observations of moving magnetic features near sunspots. *Solar Phys.* **28**, 61.

Howard, R.F.: 1990, The magnetic fields of active regions. II. Rotation. *Solar Phys.* **126**, 299.

Iijima, H., Yokoyama, T.: 2017, A three-dimensional magnetohydrodynamic simulation of the formation of solar chromospheric jets with twisted magnetic field lines. *Astrophys. J.* **848**, 38. DOI.

Jing, J., Liu, N., Lee, J., Xu, Y., Cao, W., Wang, H.: 2023, Characterizing 3D magnetic structures in sunspot light bridges. *Astrophys. J.* **952**, 40. DOI.

Kamlah, R., Verma, M., Denker, C., Wang, H.: 2023, High-resolution imaging of solar pores. *Astron. Astrophys.* **675**, A182. DOI.

Khomenko, E., Collados, M.: 2015, Oscillations and waves in sunspots. *Living Rev. Solar Phys.* **12**, 6. DOI.

Kleint, L., Berkefeld, T., Esteves, M., Sonner, T., Volkmer, R., Gerber, K., Krämer, F., Grassin, O., Berdyugina, S.: 2020, GREGOR: optics redesign and updates from 2018 – 2020. *Astron. Astrophys.* **641**, A27. DOI.

Koutchmy, S., Adjabshirzadeh, A.: 1981, Photometric analysis of the sunspot umbral dots – part two – size shape and temperature. *Astron. Astrophys.* **99**, 111.

Kuckein, C., Denker, C., Verma, M., Balthasar, H., González Manrique, S.J., Louis, R.E., Diercke, A.: 2017, STools – a data reduction pipeline for the GREGOR Fabry-Pérot interferometer and the high-resolution fast imager at the GREGOR solar telescope. In: Vargas Domínguez, S., Kosovichev, A.G., Harra, L., Antolin, P. (eds.) *Fine Structure and Dynamics of the Solar Atmosphere*, *IAU Symp* **327**, 20. DOI.

Künzel, H.: 1969, Über den Zusammenhang zwischen Penumbraformen und magnetischer Polarität sverteilung in Sonnenfleckengruppen. *Astron. Nachr.* **291**, 265.

Kutsenko, A.S., Abramenko, V.I., Litvishko, D.V.: 2023, The rotation rate of solar active and ephemeral regions. II. Temporal variations of the rotation rates. *Mon. Not. Roy. Astron. Soc.* **519**, 5315. DOI.

Lee, J.-S.: 1986, Speckle suppression and analysis for synthetic aperture radar images. *Opt. Eng.* **25**, 636. DOI.

Leenaarts, J., Carlsson, M., Rouppe van der Voort, L.: 2012, The formation of the Hα line in the solar chromosphere. *Astrophys. J.* **749**, 136. DOI.

Leka, K.D., Skumanich, A.: 1998, The evolution of pores and the development of penumbrae. *Astrophys. J.* **507**, 454. DOI.

Lemen, J.R., Title, A.M., Akin, D.J., Boerner, P.F., Chou, C., Drake, J.F., Duncan, D.W., Edwards, C.G., Friedlaender, F.M., Heyman, G.F., Hurlburt, N.E., Katz, N.L., Kushner, G.D., Levay, M., Lindgren, R.W., Mathur, D.P., McFeaters, E.L., Mitchell, S., Rehse, R.A., Schrijver, C.J., Springer, L.A., Stern, R.A., Tarbell, T.D., Wuelser, J.-P., Wolfson, C.J., Yanari, C., Bookbinder, J.A., Cheimets, P.N., Caldwell, D., Deluca, E.E., Gates, R., Golub, L., Park, S., Podgorski, W.A., Bush, R.I., Scherrer, P.H., Gummin, M.A., Smith, P., Auker, G., Jerram, P., Pool, P., Soufli, R., Windt, D.L., Beardsley, S., Clapp, M., Lang, J., Waltham, N.: 2012, The Atmospheric Imaging Assembly (AIA) on the Solar Dynamics Observatory (SDO). *Solar Phys.* **275**, 17.

Lindner, P., Kuckein, C., González Manrique, S.J., Bello González, N., Kleint, L., Berkefeld, T.: 2023, The role of the chromospheric magnetic canopy in the formation of a sunspot penumbra. *Astron. Astrophys.* **673**, A64. DOI.

Lites, B.W., Bida, T.A., Johannesson, A., Scharmer, G.B.: 1991, High-resolution spectra of solar magnetic features. II. Magnetic fields of umbral brightenings. *Astrophys. J.* **373**, 683. DOI.

Liu, S., Liu, D.: 2015, Fine magnetic characteristics of a light bridge observed by Hinode. *Adv. Space Res.* **55**, 2931. DOI.

Livingston, W.: 2002, Sunspots observed to physically weaken in 2000 – 2001. *Solar Phys.* **207**, 41. DOI.

Löfdahl, M.G.: 2002, Multi-frame blind deconvolution with linear equality constraints. In: Bones, P.J., Fiddy, M.A., Millane, R.P. (eds.) *Image Reconstruction from Incomplete Data*, *Proc. SPIE* **4792**, 146. DOI.

Lohmann, A.W., Weigelt, G., Wirnitzer, B.: 1983, Speckle masking in astronomy – triple correlation theory and applications. *Appl. Opt.* **22**, 4028. DOI.

Löhner-Böttcher, J., Schlichenmaier, R.: 2013, Correlations between sunspots and their moat flows. *Astron. Astrophys.* **551**, A105. DOI.

Márquez, I., Sánchez Almeida, J., Bonet, J.A.: 2006, High-resolution proper motions in a sunspot penumbra. *Astrophys. J.* **638**, 553.
McIntosh, P.S.: 1990, The classification of sunspot groups. *Solar Phys.* **125**, 251.
Molowny-Horas, R.: 1994, Proper motion measurements of umbral and penumbral structure. *Solar Phys.* **154**, 29.
Moore, R., Rabin, D.: 1985, Sunspots. *Annu. Rev. Astron. Astrophys.* **23**, 239.
Moore, R.L., Tang, F., Bohlin, J.D., Golub, L.: 1977, Hα macrospicules – identification with EUV macrospicules and with flares in X-ray bright points. *Astrophys. J.* **218**, 286.
Mulay, S.M., Tripathi, D., Del Zanna, G., Mason, H.: 2016, Multiwavelength study of 20 jets that emanate from the periphery of active regions. *Astron. Astrophys.* **589**, A79. DOI.
Muller, R., Mena, B.: 1987, Motions around a decaying sunspot. *Solar Phys.* **112**, 295. DOI.
Murabito, M., Romano, P., Guglielmino, S.L., Zuccarello, F., Solanki, S.K.: 2016, Formation of the penumbra and start of the evershed flow. *Astrophys. J.* **825**, 75. DOI.
Murabito, M., Guglielmino, S.L., Ermolli, I., Romano, P., Jafarzadeh, S., Rouppe van der Voort, L.H.M.: 2021, Penumbral decay observed in active region NOAA 12585. *Astron. Astrophys.* **653**, A93. DOI.
November, L.J., Simon, G.W.: 1988, Precise proper-motion measurement of solar granulation. *Astrophys. J.* **333**, 427. DOI.
Panja, M., Cameron, R.H., Solanki, S.K.: 2021, Sunspot simulations: penumbra formation and the fluting instability. *Astrophys. J.* **907**, 102. DOI.
Pesnell, W.D., Thompson, B.J., Chamberlin, P.C.: 2012, The Solar Dynamics Observatory (SDO). *Solar Phys.* **275**, 3. DOI.
Pierce, A.K., Slaughter, C.D., Weinberger, D.: 1977, Solar limb darkening. II. In the interval 7404 – 24018 Å. *Solar Phys.* **52**, 179.
Pietrow, A.G.M., Druett, M.K., de la Cruz Rodriguez, J., Calvo, F., Kiselman, D.: 2022, Physical properties of a fan-shaped jet backlit by an X9.3 flare. *Astron. Astrophys.* **659**, A58. DOI.
Quintero Noda, C., Collados, M., Regalado Olivares, S., González, F., Quintero Nehrkorn, J., Rodríguez Delgado, H., López López, R., Dominguez-Tagle, C., Mato, Á., Vaz Cedillo, J.J., Barreto Cabrera, M.: 2022, The upgraded GREGOR infrared spectrograph. In: Evans, C.J., Bryant, J.J., Motohara, K. (eds.) *Ground-Based and Airborne Instrumentation for Astronomy IX*, *Proc. SPIE* **12184**, 121840U. DOI.
Regalado Olivares, S., López López, R., González, F., Collados, M., Dominguez-Tagle, C., Mato Martínez, Á., Vaz Cedillo, J.J., Quintero Noda, C., Quintero Nehrkorn, J., Rodriguez Delgado, H., Barreto, M.: 2022, Optical and mechanical updates in the GREGOR infrared spectrograph for simultaneous spectral observations. In: Navarro, N., Geyl, R. (eds.) *Advances in Optical and Mechanical Technologies for Telescopes and Instrumentation V*, *Proc. SPIE* **12188**, 121885B. DOI.
Rempel, M.: 2015, Numerical simulations of sunspot decay: on the penumbra-evershed flow-moat flow connection. *Astrophys. J.* **814**, 125. DOI.
Riethmüller, T.L., Solanki, S.K., Zakharov, V., Gandorfer, A.: 2008, Brightness, distribution, and evolution of sunspot umbral dots. *Astron. Astrophys.* **492**, 233. DOI.
Romano, P., Frasca, D., Guglielmino, S.L., Ermolli, I., Tritschler, A., Reardon, K.P., Zuccarello, F.: 2013, Velocity and magnetic field distribution in a forming penumbra. *Astrophys. J. Lett.* **771**, L3.
Romano, P., Guglielmino, S.L., Cristaldi, A., Ermolli, I., Falco, M., Zuccarello, F.: 2014, Evolution of the magnetic field inclination in a forming penumbra. *Astrophys. J.* **784**, 10. DOI.
Romano, P., Murabito, M., Guglielmino, S.L., Zuccarello, F., Falco, M.: 2020, Restoring process of sunspot penumbra. *Astrophys. J.* **899**, 129. DOI.
Roy, J.R.: 1973, The magnetic properties of solar surges. *Solar Phys.* **28**, 95. DOI.
Rucklidge, A.M., Schmidt, H.U., Weiss, N.O.: 1995, The abrupt development of penumbrae in sunspots. *Mon. Not. Roy. Astron. Soc.* **273**, 491.
Ruiz Cobo, B., del Toro Iniesta, J.C.: 1992, Inversion of Stokes profiles. *Astrophys. J.* **398**, 375.
Sánchez Almeida, J., Asensio Ramos, A., Trujillo Bueno, J., Cernicharo, J.: 2001, G-band spectral synthesis in solar magnetic concentrations. *Astrophys. J.* **555**, 978.
Scherrer, P.H., Schou, J., Bush, R.I., Kosovichev, A.G., Bogart, R.S., Hoeksema, J.T., Liu, Y., Duvall, T.L., Zhao, J., Title, A.M., Schrijver, C.J., Tarbell, T.D., Tomczyk, S.: 2012, The Helioseismic and Magnetic Imager (HMI) Investigation for the Solar Dynamics Observatory (SDO). *Solar Phys.* **275**, 207.
Schmidt, W., Stix, M., Wöhl, H.: 1999, Center-to-limb variation of the solar oscillation. New results from MDI data. *Astron. Astrophys.* **346**, 633.
Schmidt, W., von der Lühe, O., Volkmer, R., Denker, C., Solanki, S.K., Balthasar, H., Bello Gonzalez, N., Berkefeld, T., Collados, M., Fischer, A., Halbgewachs, C., Heidecke, F., Hofmann, A., Kneer, F., Lagg, A., Nicklas, H., Popow, E., Puschmann, K.G., Schmidt, D., Sigwarth, M., Sobotka, M., Soltau, D., Staude, J., Strassmeier, K.G., Waldmann, T.A.: 2012, The 1.5 meter solar telescope GREGOR. *Astron. Nachr.* **333**, 796.

Schou, J., Scherrer, P.H., Bush, R.I., Wachter, R., Couvidat, S., Rabello-Soares, M.C., Bogart, R.S., Hoeksema, J.T., Liu, Y., Duvall, T.L., Akin, D.J., Allard, B.A., Miles, J.W., Rairden, R., Shine, R.A., Tarbell, T.D., Title, A.M., Wolfson, C.J., Elmore, D.F., Norton, A.A., Tomczyk, S.: 2012, Design and ground calibration of the Helioseismic and Magnetic Imager (HMI) instrument on the Solar Dynamics Observatory (SDO). *Solar Phys.* **275**, 229.

Sheeley, N.R. Jr.: 1972, Observations of the horizontal velocity field surrounding sunspots. *Solar Phys.* **25**, 98.

Shimizu, T., Ichimoto, K., Suematsu, Y.: 2012, Precursor of sunspot penumbral formation discovered with Hinode solar optical telescope observations. *Astrophys. J. Lett.* **747**, L18. DOI.

Shine, R.A., Title, A., Frank, Z., Scharmer, G.: 1996, Photospheric surface flows and small magnetic structures in sunspot moats. *Astron. Astrophys. Suppl. Ser.* **28**, 871.

Sobotka, M., Brandt, P.N., Simon, G.W.: 1997, Fine structure in sunspots. I. Sizes and lifetimes of umbral dots. *Astron. Astrophys.* **328**, 682.

Sobotka, M., Roudier, T.: 2007, Properties of sunspot moats derived from horizontal motions. *Astron. Astrophys.* **472**, 277.

Solanki, S.K.: 1993, Smallscale solar magnetic fields – an overview. *Space Sci. Rev.* **63**, 1. DOI.

Solanki, S.K.: 2003, Sunspots: an overview. *Astron. Astrophys. Rev.* **11**, 153.

Staude, J.: 1999, Sunspot oscillations. In: Schmieder, B., Hofmann, A., Staude, J. (eds.) *Third Advances in Solar Physics Euroconference: Magnetic Fields and Oscillations*, *ASP Conf. Ser.* **184**, 113.

Sütterlin, P.: 1998, Properties of solar pores. *Astron. Astrophys.* **333**, 305.

Tsiropoula, G., Tziotziou, K., Kontogiannis, I., Madjarska, M.S., Doyle, J.G., Suematsu, Y.: 2012, Solar fine-scale structures. I. Spicules and other small-scale, jet-like events at the chromospheric level: observations and physical parameters. *Space Sci. Rev.* **169**, 181. DOI.

van Noort, M., Rouppe van der Voort, L., Löfdahl, M.G.: 2005, Solar image restoration by use of multi-frame blind deconvolution with multiple objects and phase diversity. *Solar Phys.* **228**, 191. DOI.

Vargas Domínguez, S., Rouppe van der Voort, L., Bonet, J.A., Martínez Pillet, V., Van Noort, M., Katsukawa, Y.: 2008, Moat flow in the vicinity of sunspots for various penumbral configurations. *Astrophys. J.* **679**, 900.

Verma, M.: 2018, The origin of two X-class flares in active region NOAA 12673. Shear flows and head-on collision of new and preexisting flux. *Astron. Astrophys.* **612**, A101. DOI.

Verma, M., Denker, C.: 2011, Horizontal flow fields observed in Hinode G-band images. I. Methods. *Astron. Astrophys.* **529**, A153.

Verma, M., Denker, C.: 2014, Horizontal flow fields observed in Hinode G-band images. IV. Statistical properties of the dynamical environment around pores. *Astron. Astrophys.* **563**, A112. DOI.

Verma, M., Kummerow, P., Denker, C.: 2018, On the extent of the moat flow in axisymmetric sunspots. *Astron. Nachr.* **339**, 268. DOI.

Verma, M., Steffen, M., Denker, C.: 2013, Evaluating local correlation tracking using CO5BOLD simulations of solar granulation. *Astron. Astrophys.* **555**, A136.

Verma, M., Balthasar, H., Deng, N., Liu, C., Shimizu, T., Wang, H., Denker, C.: 2012, Horizontal flow fields observed in Hinode G-band images. II. Flow fields in the final stages of sunspot decay. *Astron. Astrophys.* **538**, A109.

Verma, M., Denker, C., Böhm, F., Balthasar, H., Fischer, C.E., Kuckein, C., Bello González, N., Berkefeld, T., Collados, M., Diercke, A., Feller, A., González Manrique, S.J., Hofmann, A., Lagg, A., Nicklas, H., Orozco Suárez, D., Pator Yabar, A., Rezaei, R., Schlichenmaier, R., Schmidt, D., Schmidt, W., Sigwarth, M., Sobotka, M., Solanki, S.K., Soltau, D., Staude, J., Strassmeier, K.G., Volkmer, R., von der Lühe, O., Waldmann, T.: 2016, Flow and magnetic field properties in the trailing sunspots of active region NOAA 12396. *Astron. Nachr.* **337**, 1090. DOI.

Verma, M., Denker, C., Balthasar, H., Kuckein, C., Rezaei, R., Sobotka, M., Deng, N., Wang, H., Tritschler, A., Collados, M., Diercke, A., Manrique, S.J.G.: 2018, High-resolution imaging and near-infrared spectroscopy of penumbral decay. *Astron. Astrophys.* **614**, A2. DOI.

Verma, M., Denker, C., Diercke, A., Kuckein, C., Balthasar, H., Dineva, E., Kontogiannis, I., Pal, P.S., Sobotka, M.: 2020, High-resolution spectroscopy of a surge in an emerging flux region. *Astron. Astrophys.* **639**, A19. DOI.

von der Lühe, O.: 1993, Speckle imaging of solar small scale structure. I. Methods. *Astron. Astrophys.* **268**, 374.

Wang, H., Johannesson, A., Stage, M., Lee, C., Zirin, H.: 1998, Study of Hα jets on the quiet sun. *Solar Phys.* **178**, 55.

Wang, J., Liu, C., Deng, N., Wang, H.: 2018, Evolution of photospheric flow and magnetic fields associated with the 2015 June 22 M6.5 flare. *Astrophys. J.* **853**, 143. DOI.

Watanabe, H., Kitai, R., Otsuji, K.: 2014, Formation and decay of rudimentary penumbra around a pore. *Astrophys. J.* **796**, 77. DOI.

Weigelt, G., Wirnitzer, B.: 1983, Image reconstruction by the speckle-masking method. *Opt. Lett.* **8**, 389. DOI.

Wöger, F., von der Lühe, O.: 2008, KISIP: a software package for speckle interferometry of adaptive optics corrected solar data. In: Bridger, A., Radziwill, N.M. (eds.) *Advanced Software and Control for Astronomy II*, *Proc. SPIE* **7019**, 70191E. DOI.

Wöger, F., von der Lühe, O., Reardon, K.: 2008, Speckle interferometry with adaptive optics corrected solar data. *Astron. Astrophys.* **488**, 375. DOI.